Rab3-interacting molecules 2α and 2β promote the abundance of voltage-gated $Ca_V1.3$ Ca^{2+} channels at hair cell active zones

Sangyong Jung[a,b,1], Tomoko Oshima-Takago[a,c,1], Rituparna Chakrabarti[c,d,e,2], Aaron B. Wong (黃沛燊)[a,c,e,2,3], Zhizi Jing[c,e,f], Gulnara Yamanbaeva[c,e,f], Maria Magdalena Picher[c,e,g], Sonja M. Wojcik[h], Fabian Göttfert[c,i], Friederike Predoehl[a], Katrin Michel[j,k], Stefan W. Hell[b,i], Susanne Schoch[j,k], Nicola Strenzke[e,f,4], Carolin Wichmann[d,e,4], and Tobias Moser[a,b,e,g,4]

[a]Institute for Auditory Neuroscience and InnerEarLab, University Medical Center Göttingen, 37099 Göttingen, Germany; [b]Center for Nanoscale Microscopy and Molecular Physiology of the Brain, University of Göttingen, 37099 Göttingen, Germany; [c]Sensory and Motor Neuroscience Program, Göttingen Graduate School for Neurosciences, Biophysics and Molecular Biosciences, University of Göttingen, 37099 Göttingen, Germany; [d]Molecular Architecture of Synapses Group, Institute for Auditory Neuroscience and InnerEarLab, University Medical Center Göttingen, 37099 Göttingen, Germany; [e]Collaborative Sensory Research Center 889, University of Göttingen, 37099 Göttingen, Germany; [f]Auditory Systems Physiology Group, InnerEarLab, Department of Otolaryngology, University of Göttingen Medical Center, 37099 Göttingen, Germany; [g]Bernstein Center for Computational Neuroscience, University of Göttingen, 37073 Göttingen, Germany; [h]Department of Molecular Neurobiology, Max Planck Institute for Experimental Medicine, 37075 Göttingen, Germany; [i]Department of Nanobiophotonics, Max Planck Institute for Biophysical Chemistry, 37077 Göttingen, Germany; [j]Institute of Neuropathology, University of Bonn, 53111 Bonn, Germany; and [k]Department of Epileptology, University of Bonn, 53111 Bonn, Germany

Edited by Thomas C. Südhof, Stanford University School of Medicine, Stanford, CA, and approved May 6, 2015 (received for review September 7, 2014)

Ca^{2+} influx triggers the fusion of synaptic vesicles at the presynaptic active zone (AZ). Here we demonstrate a role of Ras-related in brain 3 (Rab3)–interacting molecules 2α and β (RIM2α and RIM2β) in clustering voltage-gated $Ca_V1.3$ Ca^{2+} channels at the AZs of sensory inner hair cells (IHCs). We show that IHCs of hearing mice express mainly RIM2α, but also RIM2β and RIM3γ, which all localize to the AZs, as shown by immunofluorescence microscopy. Immunohistochemistry, patch-clamp, fluctuation analysis, and confocal Ca^{2+} imaging demonstrate that AZs of RIM2α-deficient IHCs cluster fewer synaptic $Ca_V1.3$ Ca^{2+} channels, resulting in reduced synaptic Ca^{2+} influx. Using superresolution microscopy, we found that Ca^{2+} channels remained clustered in stripes underneath anchored ribbons. Electron tomography of high-pressure frozen synapses revealed a reduced fraction of membrane-tethered vesicles, whereas the total number of membrane-proximal vesicles was unaltered. Membrane capacitance measurements revealed a reduction of exocytosis largely in proportion with the Ca^{2+} current, whereas the apparent Ca^{2+} dependence of exocytosis was unchanged. Hair cell-specific deletion of all RIM2 isoforms caused a stronger reduction of Ca^{2+} influx and exocytosis and significantly impaired the encoding of sound onset in the postsynaptic spiral ganglion neurons. Auditory brainstem responses indicated a mild hearing impairment on hair cell-specific deletion of all RIM2 isoforms or global inactivation of RIM2α. We conclude that RIM2α and RIM2β promote a large complement of synaptic Ca^{2+} channels at IHC AZs and are required for normal hearing.

Rab3-interacting molecule | active zone | ribbon synapse | Ca^{2+} channel | vesicle

Tens of $Ca_V1.3$ Ca^{2+} channels are thought to cluster within the active zone (AZ) membrane underneath the presynaptic density of inner hair cells (IHCs) (1–4). They make up the key signaling element, coupling the sound-driven receptor potential to vesicular glutamate release (5–7). The mechanisms governing the number of Ca^{2+} channels at the AZ as well as their spatial organization relative to membrane-tethered vesicles are not well understood. Disrupting the presynaptic scaffold protein Bassoon diminishes the numbers of Ca^{2+} channels and membrane-tethered vesicles at the AZ (2, 8). However, the loss of Bassoon is accompanied by the loss of the entire synaptic ribbon, which makes it challenging to distinguish the direct effects of gene disruption from secondary effects (9).

Among the constituents of the cytomatrix of the AZ, RIM1 and RIM2 proteins are prime candidates for the regulation of Ca^{2+} channel clustering and function (10, 11). The family of RIM proteins has seven identified members (RIM1α, RIM1β, RIM2α, RIM2β, RIM2γ, RIM3γ, and RIM4γ) encoded by four genes (RIM1–RIM4). All isoforms contain a C-terminal C_2 domain but differ in the presence of additional domains. RIM1 and RIM2 interact with Ca^{2+} channels, most other proteins of the cytomatrix of the AZ, and synaptic vesicle proteins. They interact directly with the auxiliary β (Ca_Vβ) subunits (12, 13) and pore-forming Ca_Vα subunits (14, 15). In addition, RIMs are indirectly linked to Ca^{2+} channels via RIM-binding protein (14, 16, 17). A regulation of biophysical channel properties has been demonstrated in heterologous expression systems for RIM1 (12) and RIM2 (13).

Significance

Sound encoding relies on Ca^{2+}-regulated transmitter release from inner hair cells (IHCs). Here we demonstrate a role of Ras-related in brain 3 (Rab3)–interacting molecule 2 (RIM2) in Ca^{2+} channel-clustering and vesicle-tethering at the active zones of IHCs. Active zones of RIM2α-deficient IHCs cluster fewer synaptic voltage-gated $Ca_V1.3$ Ca^{2+} channels, resulting in reduced synaptic Ca^{2+} influx. Exocytosis was diminished in RIM2α-deficient IHCs, likely contributing to the mild hearing impairment of RIM2α knockout mice. Hair cell-specific disruption of all RIM2 isoforms caused a stronger decrease of Ca^{2+} current and exocytosis in IHCs and impaired the encoding of sound onset in spiral ganglion neurons. We conclude that RIM2α and RIM2β promote synaptic clustering of Ca^{2+} channels at IHC active zones and are required for normal hearing.

Author contributions: S.J., T.O.-T., N.S., C.W., and T.M. designed research; S.J., T.O.-T., R.C., A.B.W., Z.J., G.Y., M.M.P., F.G., F.P., N.S., C.W., and T.M. performed research; S.M.W., K.M., S.W.H., and S.S. contributed new reagents/analytic tools; S.M.W. and S.S. provided animals; K.M. provided antibody; S.J., R.C., A.B.W., Z.J., G.Y., F.G., F.P., and N.S. analyzed data; and S.J., N.S., C.W., and T.M. wrote the paper.

The authors declare no conflict of interest.

This article is a PNAS Direct Submission.

[1]S.J. and T.O.-T. contributed equally to this work.

[2]R.C. and A.B.W. contributed equally to this work.

[3]Present address: Department of Neuroscience, Erasmus MC, NL-3015 CN Rotterdam, The Netherlands.

[4]To whom correspondence may be addressed. Email: tmoser@gwdg.de, NStrenzke@med.uni-goettingen.de, or cwichma@gwdg.de.

This article contains supporting information online at www.pnas.org/lookup/suppl/doi:10.1073/pnas.1417207112/-/DCSupplemental.

A role of RIM1 and RIM2 in clustering Ca^{2+} channels at the AZ was demonstrated by analysis of RIM1/2-deficient presynaptic terminals of cultured hippocampal neurons (14), auditory neurons in slices (18), and *Drosophila* neuromuscular junction (19). Because α-RIMs also bind the vesicle-associated protein Ras-related in brain 3 (Rab3) via the N-terminal zinc finger domain (20), they are also good candidates for molecular coupling of Ca^{2+} channels and vesicles (18, 21, 22). Finally, a role of RIMs in priming of vesicles for fusion is the subject of intense research (18, 21–27). RIMs likely contribute to priming via disinhibiting Munc13 (26) and regulating vesicle tethering (27). Here, we studied the expression and function of RIM in IHCs. We combined molecular, morphologic, and physiologic approaches for the analysis of RIM2α knockout mice [RIM2α SKO (28); see *Methods*] and of hair cell-specific RIM1/2 knockout mice (RIM1/2 cDKO). We demonstrate that RIM2α and RIM2β are present at IHC AZs of hearing mice, positively regulate the number of synaptic $Ca_V1.3$ Ca^{2+} channels, and are required for normal hearing.

Results

RIM2α, RIM2β, and RIM3γ Are Present at IHC AZs of Hearing Mice. The mature IHC ribbon synapse shows an unconventional molecular composition (reviewed in refs. 29–31). Recently, the expression of RIM2 and its colocalization with synaptic ribbons was demonstrated for immature mouse IHCs. However, IHCs of hearing mice were reported to lack RIM2 protein as well as RIM1–RIM4 mRNA (13). Here we revisited the expression of RIMs in IHCs of hearing mice, using RT-PCR and immunohistochemistry, using knockout tissue as control. We used the previously published conditional RIM1/2 DKO (14) and crossed it to a new transgenic mouse line expressing Cre-recombinase under the promoter of *Vglut3* [Vglut3-Cre, generated as described in *SI Appendix*, Fig. S1*A*, active in IHCs (31, 32); a detailed characterization of the Vglut3-Cre line will be published as a separate study] for hair cell-specific deletion of all RIM1 and RIM2 isoforms (nicknamed RIM1/2 cDKO). Using a floxed-GFP reporter (33), Cre recombination was observed in >99% of IHCs and in some outer hair cells, but not in neurons or supporting cells within the cochlea (*SI Appendix*, Fig. S1*B*). Different from a previous report (13), we detected mRNA for RIM1–RIM4 in organs of Corti of wild-type mice after the onset of hearing [*SI Appendix*, Fig. S2*A* and *SI Appendix*, Experimental Procedures, postnatal day (p) 14–16, not differentiating the individual RIM1/2 isoforms]. Nested RT-PCR revealed RIM2 and RIM3γ mRNA in single IHCs (p14–p16; *SI Appendix*, Fig. S2*B*). Nested RT-PCR for specific RIM2-isoforms detected RIM2α mRNA in most IHCs (*SI Appendix*, Fig. S2*C*). mRNAs for RIM2β and RIM2γ were more rarely detectable in single IHCs but were always found at the organ of Corti level (*SI Appendix*, Fig. S2*C*).

Next, we studied the presence and localization of RIM proteins by labeling IHCs of wild-type, RIM2α SKO, and RIM1/2 cDKO mice with antibodies to RIM1, RIM2, and RIM3γ. In wild-type IHCs, we found spot-like RIM2 (Fig. 1*A*) and RIM3γ (*SI Appendix*, Fig. S3*A*) immunofluorescence that colocalized with C-terminal binding protein 2 (CtBP2)/RIBEYE–marked ribbon-occupied AZ of IHCs, whereas no obvious RIM1 immunofluorescence was detectable (*SI Appendix*, Fig. S3*B*). In addition, we found RIM2 immunofluorescence separated from ribbons (Fig. 1 *A* and *C*–*F*). This most likely reflects RIM2 expression at synapsin-expressing conventional efferent synapses (blue in Fig. 1*A*, synapsin is absent from IHCs) (34) of lateral olivocochlear neurons with spiral ganglion neurons (SGNs; connectivity is illustrated in Fig. 1*B*) underneath the IHCs (Fig. 1*D*). Using two-color stimulated emission depletion (STED) microscopy, we observed a stripe-like shape of the RIM2 immunofluorescence, which, according to synapse orientation, appeared to mark the base of the synaptic ribbon (Fig. 1*C*), indicating that RIM2 is part of the Bassoon-positive

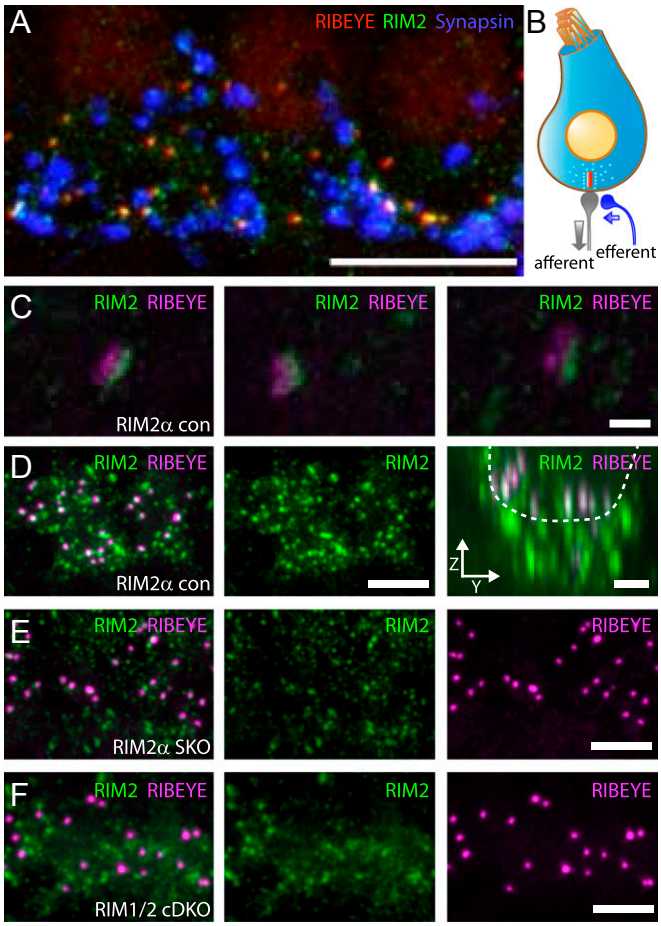

Fig. 1. RIM2α, RIM2β, and RIM3γ are present at IHC AZs of hearing mice. (*A*) Projections of confocal sections of a wild-type organ of Corti immunolabeled with antibodies to RIM2 (green), CtBP2/RIBEYE (red, antibody labeling the presynaptic ribbon), and synapsin1/2 (blue, labeling conventional efferent presynaptic terminals). Each ribbon synapse also showed RIM2-immunofluorescence, indicating the presence of RIM2 at the ribbon-type AZ of IHCs. RIM2 spots were also present away from ribbon often colocalizing with the synapsin-stain of efferent synapses onto the postsynaptic boutons of type I SGNs formed by lateral olivocochlear neurons, illustrated in the simplifying schematic in *B*. (Scale bar: 10 μm.) (*C*) 2-color STED image of a wild-type IHC AZ immunolabeled for RIM2 (green) and CtBP2/RIBEYE (magenta), showing a stripe-like morphology of the synaptic RIM2 cluster that is juxtaposed to the ribbon, as expected for a protein of the presynaptic density. The image is a maximum-intensity projection after smoothing with a Gaussian (σ = 1 pixel) in ImageJ. (Scale bar: 1 μm.) (*D*) XY-projection of confocal sections of a RIM2α con organ of Corti immunolabeled with a RIM2-specific antibody (green, *Middle*) and a CtBP2/RIBEYE antibody labeling the presynaptic ribbon (magenta, merged with green, *Left*). (*Right*) ZY projections of the same confocal sections with two IHCs (basolateral pole outlined by dashed line) illustrating RIM2 immunofluorescence underneath the IHCs. [Scale bars: 10 μm (*Middle*), 2 μm (*Right*).] (*E*) XY projection of confocal sections of a RIM2α SKO organ of Corti immunolabeled with a RIM2-specific antibody (green, *Middle*) and a CtBP2/RIBEYE antibody labeling the presynaptic ribbon (magenta, *Right*). Each ribbon also showed RIM2-immunofluorescence, indicating the presence of RIM2β at the ribbon-type AZ of RIM2α SKO IHCs. (Scale bar: 10 μm.) (*F*) XY projection of confocal sections of a RIM1/2 cDKO organ of Corti immunolabeled with a RIM2-specific antibody (green, *Middle*) and a CtBP2/RIBEYE antibody labeling the presynaptic ribbon (magenta, *Right*). RIM2 spots were always separated from ribbons, consistent with RIM2 expression at efferent synapses in the hair cell-specific cDKO. (Scale bar: 10 μm.)

presynaptic density of the AZ, which occupies the space between the ribbon and membrane (4). RIM2 immunofluorescence,

although weaker, remained at the ribbon-occupied AZs of RIM2α SKO IHCs (Fig. 1*E*) but was absent from AZs of IHCs of RIM1/2 cDKO mice lacking all RIM2 isoforms (Fig. 1*F*). This indicates the additional presence of RIM2β at IHC AZs, as the RIM2 antibody does not recognize RIM2γ.

Reduced $Ca_V1.3$ Ca^{2+} Channel Immunofluorescence at AZs of RIM2α-Deficient IHCs. First, we studied the role of RIM2α, the likely most abundant RIM2 isoform in IHCs, in regulating presynaptic $Ca_V1.3$ Ca^{2+} influx. We approached the overall organization of RIM2α SKO IHC synapses using immunohistochemistry for $Ca_V1.3$ and CtBP2/RIBEYE, marking the presynaptic Ca^{2+} channel cluster and ribbons as well as GluA2/3, indicating the postsynaptic AMPA receptor cluster. Ribbon-occupied synapses, identified as CtBP2/RIBEYE immunofluorescent spots juxtaposed to GluA2/3 immunofluorescence (Fig. 2*A*), were found in normal number in RIM2α SKO IHCs (Fig. 2*B*). $Ca_V1.3$ Ca^{2+} channels remained clustered at each ribbon-type IHC AZ (Fig. 2 *C* and *D*), but the $Ca_V1.3$ immunofluorescence intensity was reduced in RIM2α SKO IHCs. Using semiquantitative immunohistochemistry with identical and parallel tissue processing, imaging, and analysis of immunofluorescence, we found a reduction by 48% (Fig. 2 *D* and *E*; $P < 0.001$, 417 RIM2α SKO AZs in 56 IHCs in three organs of Corti from two mice; 390 RIM2α control (con) AZs in 50 IHCs in four organs of Corti from three mice). A similar result was obtained in two further sets of experiments. Using two-color STED microscopy, we found stripe-like Ca^{2+} channel clusters at ribbon-occupied RIM2α SKO AZs, which, on inspection, in single XY sections, seemed to be qualitatively comparable in size and shape to those of RIM2α con IHCs (Fig. 2*C*). We did not detect significant differences in immunofluorescence intensity for RIBEYE (Fig. 2*D*; $P = 0.27$, same AZs analyzed as for $Ca_V1.3$ earlier) and GluA2/3 ($P = 0.26$; $n = 650$ synapses in 72 IHCs in four organs of Corti from RIM2α SKO mice; $n = 673$ synapses in 78 IHCs and four organs of Corti for RIM2α con).

Disruption of RIM2α and RIM2β Reduces Synaptic Ca^{2+} Influx in IHCs. To study the effect of RIM2 disruption on presynaptic Ca^{2+} influx, we performed perforated patch-clamp recordings of Ca^{2+} current (I_{Ca}) and confocal imaging of presynaptic Ca^{2+} signals in IHCs of RIM2α SKO. We found a mild reduction of the whole-cell I_{Ca} amplitude on deletion of RIM2α (16.8%; Fig. 3 *A* and *B*). The deletion of all RIM2 isoforms in IHCs of RIM1/2 cDKO mice decreased I_{Ca} by 51.4% (Fig. 3*A* and *SI Appendix*, Fig. S5*C*; $P = 0.01$ relative to Cre-negative littermate controls: RIM1/2 con). I_{Ca} amplitudes were not significantly different between IHCs of RIM1/2 cDKO (lacking all RIM1 and RIM2 isoforms, eight IHCs in five organs of Corti) and RIM2 cSKO [lacking all RIM2 isoforms (see *Methods*) seven IHCs in four organs of Corti; $P = 0.5$; *SI Appendix*, Fig. S5*C*], supporting the notion that IHC AZs operate without RIM1. Next, we performed a detailed analysis of the biophysical properties of the Ca^{2+} channels in RIM2α SKO IHCs. Voltage dependence ($V_{0.5}$, −14.8 ± 2.7 mV for nine RIM2α SKO IHCs vs. −12.4 ± 3.5 mV for eight RIM2α con IHCs; $P = 0.58$) and kinetics of activation of I_{Ca} as well as I_{Ca} inactivation were unaltered (*SI Appendix*, Fig. S4 *A* and *B*). The reduced synaptic $Ca_V1.3$ immunofluorescence in RIM2α SKO IHCs suggested a diminished number of synaptic $Ca_V1.3$ Ca^{2+} channels. To test this hypothesis and probe for potential changes in single-channel current or open probability, we performed a nonstationary fluctuation analysis as described (Fig. 3*B*) (35). The estimated number of Ca^{2+} channels in RIM2α SKO IHCs (eight IHCs) amounted to 1,102 ± 65, which was 17.8% less than in RIM2α con IHCs (1,341 ± 73; seven IHCs), and hence, the reduced number of Ca^{2+} channels accounts for the reduction of the whole-cell Ca^{2+} current. Neither the single channel current nor the open probability changed significantly (*SI Appendix*, Table S3).

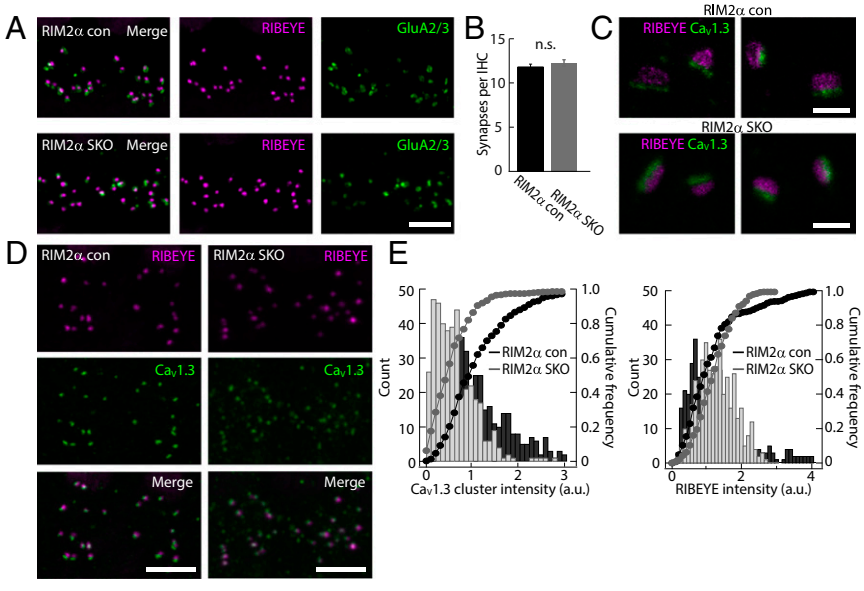

Fig. 2. Disruption of RIM2α reduces the synaptic $Ca_V1.3$ Ca^{2+} immunofluorescence. (*A*) Representative projections of confocal images showing GluA2/3 (green) and RIBEYE (magenta) across the basal region of rows of RIM2α con (*Top*) and RIM2α SKO (*Bottom*) IHCs. Orderly juxtaposed presynaptic ribbons and postsynaptic AMPA receptor clusters indicate intact ribbon-anchorage. (Scale bar: 10 μm.) (*B*) Average number of ribbon-occupied IHC synapses: comparable number of synapses in both genotypes. (*C*) Two-color STED image of immunolabeled ribbons (CtBP2/RIBEYE, magenta) and $Ca_V1.3$ channel clusters (green) in RIM2α con and RIM2α SKO IHCs. $Ca_V1.3$ channel clusters retain the stripe-like morphology. The images are maximum-intensity projections after smoothing with a Gaussian (σ = 1 pixel) in ImageJ. (Scale bar: 1 μm.) (*D*) Organs of Corti from RIM2α con (*Left*) and RIM2α SKO (*Right*) mice immunolabeled for $Ca_V1.3$ (green) and CtBP2/RIBEYE (magenta). Clusters of $Ca_V1.3$ were concentrated in the basal poles near synaptic ribbons in IHCs of both genotypes: each synaptic ribbon was accompanied by a cluster of $Ca_V1.3$. (Scale bars: 10 μm.) (*E*) Quantification of synaptic $Ca_V1.3$ immunofluorescence revealed a reduction in intensity for AZs of RIM2α SKO IHCs (*Left*), no change in CtBP2/RIBEYE immunofluorescence (*Right*).

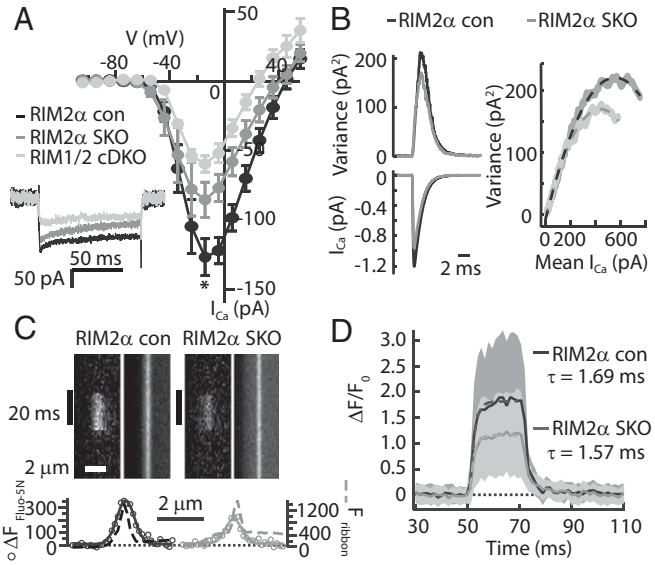

Fig. 3. Disruption of RIM2 reduces synaptic Ca^{2+} influx in IHCs. (*A*) Representative Ca^{2+} currents of a RIM 1/2 cDKO (light gray), a RIM2α SKO IHC (dark gray), and a RIM2α con IHC (black) in response to 100-ms long-step depolarizations to −14 mV. Average steady-state I_{Ca}-V of RIM 1/2 cDKO (light gray, $n = 8$), RIM2α SKO (gray, $n = 9$), and RIM2α con (black, $n = 8$) IHCs acquired with 10-ms-long depolarizations (steady-state Ca^{2+} current during depolarization): comparable voltage dependence, but reduction of amplitude in RIM2-deficient IHCs. (*B*) Exemplary mean Ca^{2+} tail-currents (*Lower left*) and corresponding trial-to-trial variance (*Upper left*) used for nonstationary fluctuation analysis (*SI Appendix*, Table S3), elicited by repolarizing IHCs from +57 mV to −68 mV. $[Ca^{2+}]_e$ = 10 mM, $[BayK8644]_e$ = 5 µM. (*Right*) Representative variance vs. mean relationships of RIM2α SKO (gray) and RIM2α con (black) IHCs. Dashed lines represent parabolic fits. (*C*) Exemplary line scans across hotspots of Ca^{2+} influx in a RIM2α SKO IHC and a RIM2α con IHC during depolarization to −7 mV for 20 ms (marked by black lines). (*Left*) Fluorescence change in the Ca^{2+} indicator (ΔF, 0.4 mM Fluo-5N, 2 mM $[EGTA]_i$). (*Right*) Fluorescence of a fluorescently tagged CtBP2-binding peptide, which labels the synaptic ribbon. (Scale bar: 2 µm.) Average ΔF of Fluo-5N (open circles) during the 20-ms depolarization, and average fluorescence of the peptide (dashed lines) before depolarization (*Bottom*), plotted as a function of position. (*Bottom*) Examples in right and left of upper, respectively. Solid lines are Gaussian fits to the ΔF data. (Scale bar: 2 µm.) (*D*) Synaptic Ca^{2+} signal displayed as baseline-normalized Fluo-5N fluorescence change ($\Delta F/F_0$) at the center of the ribbon as a function of time obtained from line scans on RIM2α SKO ($n = 40$ AZs) and RIM2α con ($n = 35$ AZs) IHCs. Thick solid lines represent the respective means, dashed lines represent single exponential fits to the means, SDs are provided in light gray (RIM2α SKO), and dark gray (RIM2α con).

Because the whole-cell recordings sum I_{Ca} of all AZs and extrasynaptic membranes, we sought to further analyze Ca^{2+} influx at the single AZ, using confocal Ca^{2+} imaging at fluorescently tagged AZs (2, 36, 37). IHCs were depolarized for 20 ms to −7 mV to fully activate Ca^{2+} channels, and Fluo-5N fluorescence was studied using line scans across the center of "Ca^{2+} microdomains" (Fig. 3 *C* and *D*), identified as hotspots of Fluo-5N fluorescence change during a preceding 254-ms depolarization. Ca^{2+} microdomains of RIM2α SKO (40 AZs in 13 IHCs in seven organs of Corti) and RIM2α con (35 AZs in 15 IHCs in seven organs of Corti) showed comparable spatial extents (Fig. 3*C* and *SI Appendix*, Fig. S5*B*) and kinetics (Fig. 3*D*). However, we found a 36% reduction of the maximal fluorescence change (Fig. 3*D* and *SI Appendix*, Fig. S5*A*; $P < 0.002$), which is less than the decrease of synaptic $Ca_V1.3$ immunofluorescence (48%) but exceeds the loss of the whole-cell Ca^{2+} current (18%). The fluorescence change varied greatly among the AZs in IHCs of RIM2α SKO mice, as previously described for wild-type IHCs (36). The coefficients of variation were comparable in both genotypes (0.65 for RIM2α con and 0.66 for RIM2α SKO IHCs), again contrasting the synaptic phenotype of Bassoon-deficient IHCs that showed reduced Ca^{2+} signaling heterogeneity. In summary, RIM2α and RIM2β promote a large complement of synaptic $Ca_V1.3$ Ca^{2+} channels. This function of RIM2 seems to involve the immobilization of the channels at the AZ, at least in addition to promoting channel trafficking to the plasma membrane, as the reduction of synaptic Ca^{2+} channels exceeded that of the whole-cell Ca^{2+} current.

Disruption of RIM2α Reduces the Fraction of Membrane-Tethered Synaptic Vesicles. Next, we studied the ultrastructure of the AZ, using electron microscopy and tomography. To obtain a close to native structural preservation, we used high-pressure freezing in combination with freeze-substitution. Tomographic reconstructions revealed that the AZ ultrastructure was generally maintained in RIM2α SKO IHCs showing normally anchored, sized [average ribbon height: 258.4 ± 24.6 nm for RIM2α con ($n = 10$ tomograms) vs. 270.2 ± 18.0 nm for RIM2α SKO ($n = 10$ tomograms); Fig. 4 *A* and *G*] and shaped synaptic ribbons with an unaltered complement of ribbon-associated synaptic vesicles (29.0 ± 3.9 for RIM2α SKO vs. 28.2 ± 3.5 for RIM2α con per tomogram, typically containing approximately half of the ribbon). The total number of membrane-proximal vesicles within 50 nm from the AZ membrane (Fig. 4*C*) was unaltered in RIM2α SKO compared with controls (8.0 ± 1.0 for RIM2α SKO vs. 6.9 ± 0.7 for RIM2α con; Fig. 4 *D* and *F*). Performing electron tomography allowed the identification of tethers to the vesicles as well as the determination of the tether length in 3D (*SI Appendix*, Fig. S6 *A* and *B*). Interestingly, the fraction of membrane-tethered vesicles (number of tethered vesicles/total number of membrane-proximal vesicles) was significantly reduced at RIM2α SKO AZs (0.24 ± 0.03 for RIM2α SKO vs. 0.41 ± 0.02 for RIM2α con; $P < 0.002$; Fig. 4 *D* and *E*), suggesting RIM2α plays a role in tethering vesicles to the AZ membrane of IHCs. The tether length, however, was unchanged (average tether length, 22.7 ± 1.6 nm for RIM2α con vs. 22.9 ± 1.5 nm for RIM2α SKO; *SI Appendix*, Fig. S6*C*).

Disruption of RIM2α and RIM2β Reduces IHC Exocytosis. How does the disruption of RIM2 affect hair cell exocytosis? The reduction of Ca^{2+} channels and the impaired vesicle tethering are likely to diminish exocytosis. Moreover, as RIM2α is a candidate for linking vesicles and Ca^{2+} channels, a potential disruption of Ca^{2+} influx–exocytosis coupling might result. We tested these hypotheses by measuring exocytic membrane capacitance changes (ΔC_m) in RIM2α SKO and RIM1/2 cDKO IHCs in response to depolarizations of various durations to the maximum Ca^{2+} current potential in perforated-patch recordings (Fig. 5 *A* and *B*). On the basis of previous work (35, 38–40), we interpret the fast and saturating component (0–20 ms depolarization duration) as exocytosis of a standing readily releasable pool (RRP) (41), and the slower component (>20 ms depolarization duration) as sustained exocytosis, primarily reflecting vesicle supply to the RRP and subsequent fusion (Fig. 5*B*). The exocytic ΔC_m, in response to 20-ms depolarization, was reduced by 36% in RIM2α SKO IHCs (14 IHCs, $P = 0.015$ relative to RIM2α con) and by 52% in RIM1/2 cDKO (15 IHCs, $P = 0.003$ relative to RIM1/2 con and $P < 0.001$ relative to RIM2α SKO). The rate of sustained exocytosis was diminished, as well [from 0.76 ± 0.14 fF/ms in RIM2α con IHCs to 0.38 ± 0.07 fF/ms in RIM2α SKO IHCs ($P = 0.02$ relative to RIM2α con) and 0.09 ± 0.02 fF/ms in RIM1/2 cDKO IHCs [$P < 0.001$ relative to RIM1/2 con (nine IHCs, 0.5 ± 0 0.08 fF/ms; $P < 0.001$ relative to RIM2α SKO)]. Exocytosis was not significantly different between IHCs of RIM1/2 cDKO and RIM2 cSKO ($P = 0.5$; *SI Appendix*, Fig. S5*D*), supporting the notion that hair cell AZ operates without RIM1. Relating the exocytic ΔC_m to the

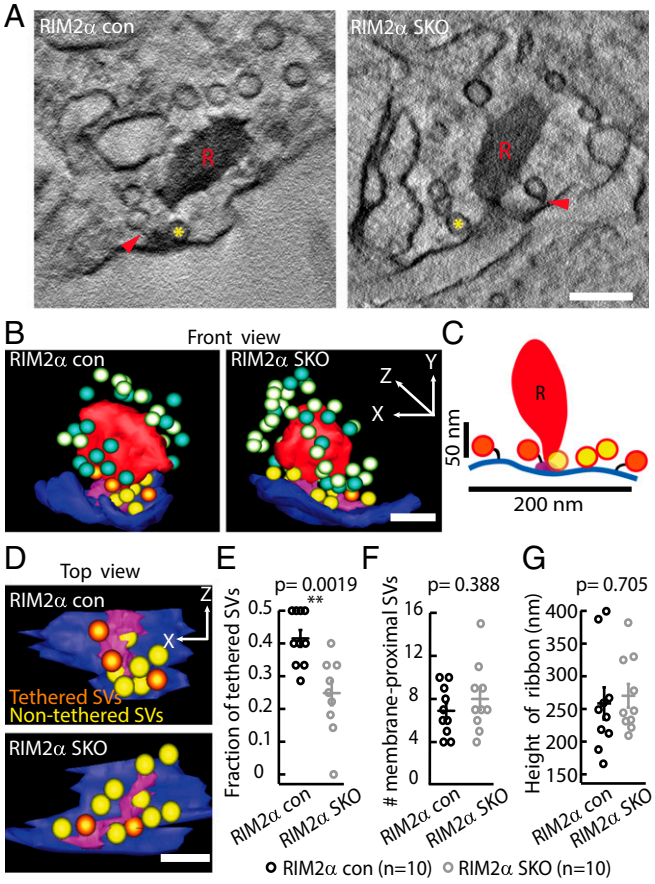

Fig. 4. Disruption of RIM2α affects the ultrastructure of IHC ribbon synapses. (*A*) Exemplary virtual electron tomographic sections of RIM2α con and RIM2α SKO ribbon synapses: normal ribbon (R) size and shape and intact anchorage in RIM2α SKO IHCs can be observed. Different classes of synaptic vesicles are found in the membrane proximity: tethered (red arrowhead) and nontethered (yellow asterisk). For RIM2α con $n = 10$ tomograms from one animal and two organs of Corti, for RIM2α SKO $n = 10$ tomograms from two animals and two organs of Corti were analyzed. (Scale bar: 100 nm.) (*B*) Front view of rendered models of whole-ribbon synapse in RIM2α con and RIM2α SKO IHCs with tethered (dark green) and nontethered (light green) synaptic vesicles in the ribbon-associated pool. Tethered (orange) and nontethered (yellow) membrane-proximal vesicles and other synaptic structures such as ribbon (red), presynaptic density (pink), and AZ membrane (blue) are indicated. For simplicity, tethers are not reconstructed. (*C*) Illustration depicting the quantification criteria of the membrane-proximal vesicle pool (not drawn to scale). (*D*) Top view of rendered models of RIM2α SKO and RIM2α con ribbon synapse AZs with tethered (orange) and nontethered (yellow) membrane-proximal vesicles. Other synaptic structures such as ribbons and ribbon-associated vesicles are removed for clarity. (Scale bar: 100 nm.) (*E*) The ratio of the number of membrane-tethered vesicles to the total number of membrane-proximal vesicles (fraction of tethered SV) is significantly reduced in RIM2α SKO IHCs. (*F*) The average number of membrane-proximal vesicles and (*G*) the ribbon height are unchanged in RIM2α SKO IHCs compared with RIM2α con.

corresponding integrated Ca^{2+} current (Q_{Ca}; Fig. 5*C*) reduced the discrepancy of the exocytic responses between the RIM2α SKO and control IHCs, indicating that the reduction of presynaptic Ca^{2+} influx explains impaired exocytosis to a large extent.

As an interaction partner of Rab3, which is present in hair cells (42), and of the $Ca_V1.3$ channel (13), RIM2α is a candidate molecular linker between Ca^{2+} channel and vesicular release site at the IHC AZ. Hence, we studied Ca^{2+} influx-exocytosis coupling by estimating the apparent Ca^{2+} cooperativity m of exocytosis upon manipulation of the single Ca^{2+} channel current via changes of $[Ca^{2+}]_e$ (Fig. 5*D*, *Upper*) and reduction of open Ca^{2+} channels by slow perfusion of the dihydropyridine channel antagonist isradipine (10 μM; Fig. 5*D*, *Lower*). We obtained m by fitting the relationship of $\Delta C_{m,20\ ms}$ and Q_{Ca} for each cell with a power function: $\Delta C_m = A(Q_{Ca})^m$ (43), and for the case of the single Ca^{2+} channel current change, we restricted fitting to the Q_{Ca} range that did not show obvious saturation of $\Delta C_{m,20\ ms}$ (4) (Fig. 5*D*). The estimates of m were statistically indistinguishable between RIM2α SKO and RIM2α con IHCs for both manipulations [isradipine, 1.58 ± 0.12 vs. 1.51 ± 0.11 ($P = 0.62$); $\Delta[Ca^{2+}]_e$, 2.63 ± 0.09 vs. 2.59 ± 0.14 ($P = 0.8$); $n = 6$ IHCs for both genotypes]. We conclude that the RIM2α disruption impairs RRP size and replenishment, but leaves Ca^{2+} influx-exocytosis coupling largely intact.

RIM2 Disruption Impairs Sound Onset Encoding. What are the consequences of RIM2 disruption for hearing? The thresholds of auditory brainstem responses (ABRs) were mildly but significantly elevated in the RIM mutants (Fig. 6 *B* and *D*; by 5 dB SPL in RIM1/2 cDKO mice and by 16 dB in RIM2α SKO mice compared with their respective littermate controls; both $P < 0.0001$). As the presence of otoacoustic emissions with normal amplitudes (*SI Appendix*, Fig. S7 *A–D*) indicates normal mechanoelectrical transduction and cochlear amplification, this suggests a synaptopathic hearing impairment (44).

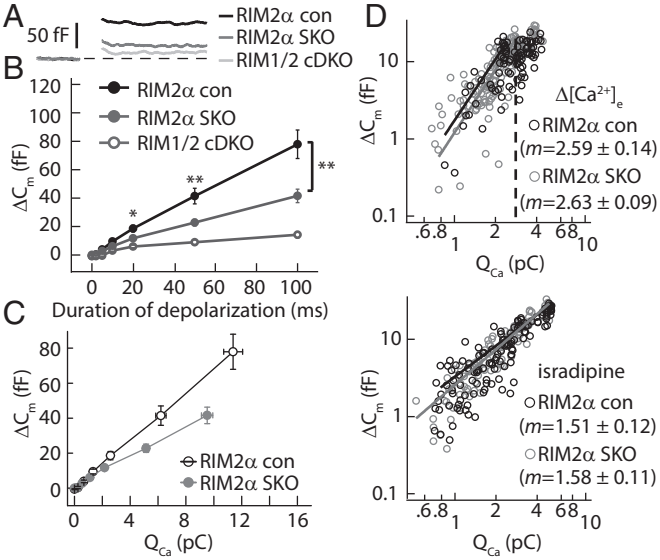

Fig. 5. Reduced exocytosis in RIM2–deficient IHCs. (*A*) Representative capacitance increments (ΔC_m) of a RIM2α SKO IHC (gray) and a RIM2α con IHC (black) in response to 100-ms long-step depolarizations to −14 mV. (*B*) Average ΔC_m of p14–p16 RIM1/2 cDKO IHCs (light gray, 10 IHCs in four organs of Corti), RIM2α SKO IHCs (dark gray, 25 IHCs in 13 organs of Corti), and RIM2α con IHCs (black, 20 IHCs in 12 organs of Corti) for depolarizations of different durations. (*C*) Average ΔC_m plotted vs. the corresponding Ca^{2+} current integral (Q_{Ca}) for RIM2α SKO IHCs and RIM2α con IHCs. ΔC_m data as in *SI Appendix*, Fig. S5*E* and binned according to duration of depolarization. (*D*, *Upper*) Apparent Ca^{2+} cooperativity of RRP exocytosis while decreasing $[Ca^{2+}]_e$. Solid lines represent best-fit power functions [$\Delta C_m = A(Q_{Ca})^m$] to the whole data set. Each small symbol represents an individual response to depolarization (seven RIM2α SKO IHCs; five RIM2α con IHCs). Dashed vertical lines indicate the average maximal Q_{Ca}, limiting the Q_{Ca} range used for fitting. (*Lower*) Apparent Ca^{2+} cooperativity of RRP exocytosis while decreasing "NxP_{open}" through blocking L-type Ca^{2+} channels with isradipine (10 μM). Each small symbol represents an individual response to 20-ms depolarization ($n = 6$, RIM2α SKO IHCs; $n = 6$, RIM2α con IHCs). Solid lines show best-fit power functions to the whole data set. Mean m and SEM were obtained from the fits to the individual IHCs.

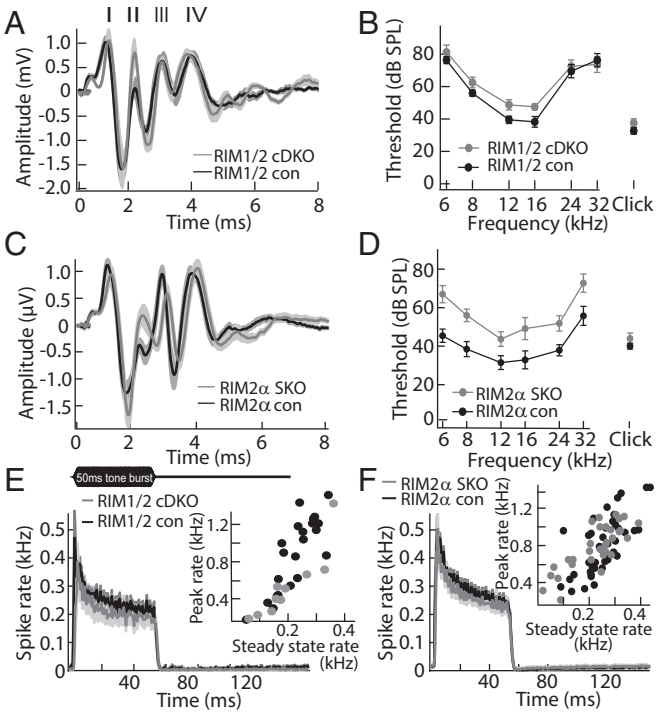

Fig. 6. Mild impairment of sound encoding in RIM1/2 cDKO and RIM2α SKO mice. (*A*) ABR waveforms of RIM1/2 cDKO mice (gray, $n = 8$) and RIM1/2 con (black, $n = 12$) in response to 80 dB (pe) click stimulation were generally preserved, but in RIM1/2 cDKO, the latency of peak I was prolonged (*SI Appendix*, Fig. S7*F*). (*B*) Average ABR thresholds of RIM1/2 cDKO mice (gray, $n = 8$) were significantly elevated compared with RIM1/2 con (black, $n = 11$). (*C*) ABR in RIM2α SKO mice (gray, $n = 15$) were preserved but had prolonged latencies of peaks II–V compared with RIM2α con (black, $n = 15$) littermate controls (*SI Appendix*, Fig. S7*E*). (*D*) Average ABR thresholds of RIM2α SKO mice (gray, $n = 11$) were significantly elevated compared with littermate controls (black, $n = 14$). (*E*) Mean peristimulus time histogram of RIM1/2 cDKO (gray, $n = 10$) and RIM1/2 con (black, $n = 22$) SGNs to tone burst stimulation at the characteristic frequency of each fiber, 30 dB above threshold. Shaded areas indicate the SEM. (*Inset*) Quantification of peak rates at sound onset (maximum, 0.5 ms bin) and steady state rates (averaged between 37 and 47 ms after sound onset) of individual fibers. Peak rates were significantly reduced in RIM1/2 cDKO ($P = 0.02$), and sustained rates tended to be reduced (n.s.); the overall response pattern was preserved. (*F*) Mean peristimulus time histogram of RIM2α SKO (gray, $n = 32$) and RIM2α con (black, $n = 42$) SGNs, illustrated as in *E*. There was a nonsignificant trend to lower spike rates in the RIM2α SKO SGNs.

The significant delay of ABR waves 2–5 (Fig. 6*C* and *SI Appendix*, Fig. S7*E*; $P < 0.0001$ for each) and the reduction in ABR wave 3 amplitude in RIM2α SKO mice (Fig. 6*D*; $P < 0.0001$) indicate an additional impairment of synaptic transmission deficit at central auditory synapses. Consistent with the above notion that the IHC synapse seems to operate without RIM1, RIM1α SKO mice showed normal ABR thresholds and waveforms (*SI Appendix*, Fig. S7 *G* and *H*), also indicating that the sole deletion of RIM1α does not impair transmission at central auditory synapses. Next, we performed extracellular recordings from individual SGNs, each of which is driven by a single AZ (45), using glass microelectrodes targeted toward the entry point of the auditory nerve into the anteroventral cochlear nucleus (46). SGNs were distinguished from cochlear nucleus neurons on the basis of their response patterns and the electrode position (*Methods*) (46). Sound thresholds (*SI Appendix*, Fig. S8*A*) and frequency tuning of SGN were comparable between RIM mutant mice and their respective littermate controls. Responses of SGNs to suprathreshold tone bursts followed an overall normal pattern, with spike rate peaking at sound onset and then gradually declining [short-term adaptation, likely reflecting partial RRP depletion (2, 46)] to an adapted rate that was maintained throughout stimulation (Fig. 6 *E* and *F*). SGNs of RIM1/2 cDKO mice showed a significantly reduced peak rate (Fig. 6*E*; $P = 0.02$, paired *t* test) and a delayed first spike latency ($P = 0.02$, paired *t* test), whereas the jitter of the first spike was unaltered ($P = 0.45$ for comparison of the variance of first spike latency). Steady-state spike rates (Fig. 6*E*) and spontaneous spike rates (*SI Appendix*, Fig. S8*B*) showed a nonsignificant trend toward smaller values. Both spontaneous (*SI Appendix*, Fig. S8*B*) and evoked rates (Fig. 6*F*) also tended to be smaller in putative SGNs of RIM2α SKO mice, although differences did not reach significance. The increase of average spike rate with sound intensity was significantly less steep, and the dynamic range tended to be broader in RIM2α SKO SGNs compared with SGNs of littermate controls (*SI Appendix*, Fig. S8 *C–E*). The time course of recovery from adaptation (likely reflecting RRP recovery from depletion; *SI Appendix*, Fig. S8*F*) was normal in RIM2α SKO SGNs, as was the temporal precision of coding, assessed as the jitter of the first spike after sound onset (*SI Appendix*, Fig. S8*G*) and as the synchronicity of firing to the sound envelope of amplitude-modulated tones (*SI Appendix*, Fig. S8*H*). Similar to SGNs, neurons of the cochlear nucleus in RIM2α SKO mice showed only subtle alterations in their spontaneous and sound-evoked spiking activity, such as a small but significant reduction of peak rates in putative bushy cells and in multipolar cells (*SI Appendix*, Fig. S8 *I* and *J*). Taken together, RIM2 disruption caused a mild sound-encoding phenotype that reached significance only in RIM1/2 cDKO SGNs, compatible with the stronger impairment of the presynaptic function of their IHCs compared with RIM2α SKO IHCs. RIM2α disruption at the central auditory synapses of RIM2α SKO mice was reflected by reduced peak firing rates in bushy cells and alteration of the central ABR peaks.

Discussion

Here we identified RIM2α and RIM2β as the long RIM isoforms at the afferent IHC synapse of hearing mice. RIM2α and RIM2β positively regulate the number of synaptic $Ca_V1.3$ Ca^{2+} channels in IHCs, likely by clustering them at the AZ. In addition, RIM2α seems to be involved in tethering synaptic vesicles to the AZ membrane. Disruption of RIM2α and RIM2β diminishes IHC exocytosis primarily via reducing synaptic Ca^{2+} influx and mildly impairs synaptic sound encoding.

AZs of Cochlear IHCs of Hearing Mice Use Multiple RIM Isoforms. The molecular composition of the IHC ribbon synapse is highly specialized to suit the needs of fast and indefatigable transmitter release and deviates from "conventional" synapses of the CNS in several ways (28–30). Here we show that IHCs of hearing mice express RIM2α, RIM2β, and RIM3γ, which corrects a previous notion of a developmental loss of RIM expression in IHCs (13). However, unlike many other synapses studied so far (14, 18, 47–49), IHC ribbon synapses seem to lack RIM1. Obviously, negative single-cell PCR and immunohistochemistry do not rule out weak RIM1 expression. However, the normal ABR in RIM1α SKO mice and the indistinguishable presynaptic dysfunction of IHCs from RIM2 cSKO and RIM1/2 cDKO mice support the notion that IHC synapses operate without RIM1. Therefore, RIM2α seems to serve as the only α-RIM capable of interacting with the vesicle-associated protein Rab3, which is also expressed in hair cells (42). Beyond the Rab3 interaction, the long isoforms RIM2α and RIM2β have overlapping interaction partners such as Munc13, ELKS, and Ca^{2+} channels. The further reduction of synaptic Ca^{2+} influx by additional deletion of RIM2β likely reflects additive and potentially nonoverlapping roles of RIM2α and RIM2β in clustering synaptic Ca^{2+} channel, although we cannot definitively exclude a compensatory up-regulation of

RIM2β in RIM2α SKO IHCs. However, neither a compensatory expression of RIM1 nor an up-regulation of RIM2β can fully substitute for the lost RIM2α in the regulation of synaptic Ca^{2+} channels in IHCs. These findings contrast recent observations at the calyx of Held synapse of the central auditory pathway, in which RIM1 and RIM2 isoforms can largely replace each other in regulating the abundance of presynaptic Ca^{2+} channels (50). The localization of RIM3γ at the IHC AZ was unexpected, given that γ-RIMs assume postsynaptic roles in CNS neurons (51, 52). Future studies on RIM3γ knockout mice will be required to confirm the specificity of RIM3γ immunolabeling at IHC AZs and to elucidate its relevance for IHC synaptic transmission and hearing.

Positive Regulation of Presynaptic Ca^{2+} Signaling of IHCs by RIM2α and RIM2β. Here we identified the IHC ribbon synapse as a system that requires RIM2α and RIM2β for normal function. Importantly, the functional synaptic deficit arose despite a normal presence of synaptic ribbons, which is different from the Bassoon disruption that also reduced synaptic Ca^{2+} channels but, in addition, impaired the anchorage of synaptic ribbons (2, 9). Immunohistochemistry and patch-clamp recordings of Ca^{2+} influx and confocal Ca^{2+} imaging consistently demonstrated a reduction of synaptic Ca^{2+} channels on disruption of RIM2α. Similar to previous findings on Bassoon-deficient IHCs (2), the reduction of synaptic Ca^{2+} channels was greater than that of the total number of channels, which likely indicates that RIM2 primarily recruits and/or retains $Ca_V1.3$ channels at the AZ. In addition, RIM2 may have a role in $Ca_V1.3$ trafficking to the plasma membrane, but the extent to which this mechanism contributes is less clear, given that palmitoylated $Ca_V\beta2a$, which is likely expressed in IHCs (35), might take this role. Unlike in Bassoon-deficient IHCs that primarily lack the population of AZs with a large Ca^{2+} channel complement (2, 9), the cumulative distribution function of $Ca_V1.3$ immunofluorescence intensities of RIM2α SKO AZs is overall shifted toward smaller values. The shape of the Ca^{2+} channel clusters at RIM2α SKO IHC AZs remained stripe-like, indicating that channel localization at the AZ is maintained on the tens of nanometer scale, whereas clusters are disintegrated into two to three round spots on Bassoon-disruption. Moreover, we found a generally well-preserved synaptic ultrastructure in IHCs of RIM2α SKO mice. Most notably, unlike the ribbonless synapses in Bassoon-deficient IHCs (8), ribbons were properly anchored and displayed a normal morphology in RIM2α-deficient IHCs. Hence, although both RIM (14, 16) and Bassoon (53) may use binding to RIM-binding protein to interact with Ca^{2+} channels, the effects of RIM2α and Bassoon disruption on $Ca_V1.3$ Ca^{2+} channel clustering at the IHC AZ differ. This may reflect a stronger perturbation of the AZ in Bassoon-deficient IHCs, which is also evident from the additional loss of the synaptic ribbon. Most likely, RIM2 also indirectly interacts with the $Ca_V1.3$ Ca^{2+} channel complex via binding to the $Ca_V\beta$ subunits (13); for instance, to $Ca_V\beta2$, the predominant β-subunit in IHCs (35). Future studies of RIM interactions with the $Ca_V1.3$ channel complex will be required to explore additional binding mechanisms and evaluate the relative contribution of the interactions for mediating the positive regulation of the number of synaptic Ca^{2+} channels by RIM2α and RIM2β.

Impaired Exocytosis and Hearing Upon RIM2 Disruption. Given the concurrent reduction of Ca^{2+} influx and exocytosis observed in the present study for both RIM2α- and RIM2α/β-deficient IHCs, we favor the interpretation that RIM2 disruption reduces exocytosis primarily by diminishing synaptic Ca^{2+} channels. The reduced presynaptic exocytosis underlies the impaired sound encoding that was more pronounced on deletion of both RIM2α and RIM2β, which also caused a stronger reduction of presynaptic Ca^{2+} influx and exocytosis. This view is in line with previous studies of IHCs with fewer channels resulting from the deletion of $Ca_V\beta2$ (35) and $Ca_V1.3\alpha$ (6), where we also observed a linear reduction of exocytosis with the Ca^{2+} current (by 70% and 90% in $Ca_V\beta2$- and $Ca_V1.3$-deficient IHCs, respectively). The apparent Ca^{2+} cooperativity of exocytosis (Fig. 5*C*) and Ca^{2+} efficiency (Fig. 5*D*) suggests that coupling of Ca^{2+} influx to exocytosis (1, 4, 54) was largely unaltered in RIM2α-deficient IHCs, which contrasts findings at the in RIM1/2-deficient IHCs calyx of Held (18), which might reflect compensation by other molecular links between channels and release sites at the IHC AZ. Alternatively, a subtle alteration of Ca^{2+} channel position relative to the vesicular Ca^{2+} sensor on the scale of few nanometers might have gone undetected in our measurements of exocytic membrane capacitance changes. Our morphological analysis did not reveal major structural deficits of RIM2α-deficient synapses: synapse number, ribbon anchorage and the shape of the Ca^{2+}channel cluster appeared intact, and the number of ribbon-associated and membrane-proximal vesicles was not changed. This contrasts the synaptic phenotype elicited by disruption of two other presynaptic scaffold proteins, CAST and Bassoon, for which a reduction in ribbon size in rod photoreceptors (55) and a loss of the ribbon, respectively, from AZs of photoreceptors (56) and hair cells (8) was reported that led to a reduction of membrane-proximal synaptic vesicles at the presynaptic AZ in each case. Our observation of a reduced fraction of membrane-tethered vesicles adds further support to a role of RIMs in regulating vesicle tethering to the membrane of the AZ (27), although RIM2α seems not to be essential for this process. The contribution of the impaired tethering to reduced exocytosis and the consequences of deleting all RIM isoforms on synaptic ultrastructure remains to be probed in future studies. Deletion of all long RIM isoforms reduced the number of docked synaptic vesicles at AZs of both cultured neonatal hippocampal neurons (14) and the calyx of Held (18). Interestingly, neither the isolated deletion of RIM1 nor RIM2 isoforms affected synaptic transmission at the calyx of Held in vitro (50), and ABR recordings suggest normal auditory signaling in RIM1α knockout mice (*SI Appendix*, Fig. S7). In contrast, delayed latencies of central auditory ABR peals and extracellular recordings from single cochlear nucleus neurons suggested a mild impairment of transmission at central auditory synapses in the absence of RIM2α. Thus, there seems to be a requirement for RIM2 at central auditory synapses for normal hearing. Future in vivo recordings from the central auditory pathway on cell-specific RIM deletion mutants will help reconciling these data sets.

Methods

Animals. Generation of RIM2α knockout mice (RIM2α SKO) (48) and conditional RIM1/2 knockout mice (RIM1/2 cDKO) (14) was described earlier. Generation of Vglut3-Cre mice is described in *SI Appendix*, Fig. S1. Most experiments compared RIM1/2 cDKO and RIM2 cSKO with their Cre-negative littermate controls (RIM1/2 con and RIM2 con), or RIM2α SKO with their wild-type littermates (RIM2α con), respectively. C57BL/6 mice were used for some experiments related to Fig. 1 and for controlling for possible effects of the Vglut3-Cre expression. All experiments complied with national animal care guidelines and were approved by the University of Göttingen Board for animal welfare and the animal welfare office of the state of Lower Saxony.

Immunohistochemistry and Immunofluorescence Microscopy. Apical cochlear turns of p14–p18 mice were fixed for 25 min in methanol at −20 °C. Primary antibodies were mouse anti-CtBP2 (1:200, BD Biosciences), rabbit anti-GluA2/3 (1:200, Chemicon), rabbit anti-$Ca_V1.3$ (1: 50, Alomone Labs), mouse anti-GluA2 (1:75 Chemicon), RIM2 (#140103 recognizing the PSD-95/discs large/ZO-1 (PDZ) domain, 1:200; Synaptic Systems), RIM1 (1:200; Synaptic Systems), RIM3 (1:100) (52), and Vglut3 (1:500; Synaptic Systems). Secondary antibodies were AlexaFluor488, 594, and 647 (1:200; Molecular Probes). Each presented immunolabeling was repeated with similar result at least three times. Images were acquired with an SP5 confocal microscope (Leica Microsystems) with a 63× oil-immersion objective (NA = 1.4). Each preparation yielded several images, each containing a row of six IHCs. For

semiquantitative analysis of immunofluorescence, samples of mutant and control were processed identically and in parallel throughout immunohistochemistry, confocal imaging, and analysis. Intensity per synapse was estimated in the optical section with peak intensity. Immunofluorescence intensity was measured as the integral of the pixel values under the 2D Gaussian after subtraction of the background [estimated by fitting a linear function to the region outside of the 2D Gaussian, and subsequently subtracting this function from the entire image (2)]. The average voxel intensity of the stack was subtracted as background. As the absolute immunofluorescence intensity varied between the sets of three ($Ca_V1.3$ and RIBEYE) and four (GluA2/3) experiments, the analysis was presented for one experiment each, but the findings in mutant relative to control were similar in all experiments.

Two-color STED images were acquired on a custom-built setup, as described previously (57). A pair of pulsed laserdiodes at 595 and 640 nm wavelength were used to excite the dyes Atto590 (Atto-Tec) and KK114 (58). The fluorescence was detected by avalanche photodiodes (SPCM-AQRH13, Excelitas, and PR-050-CTB; Micro Photon Devices) with detection windows ranging from 600 to 640 nm and from 660 to 720 nm, respectively. The resolution enhancement is achieved with a pulsed STED laser of 775 nm wavelength. As both color channels are recorded quasi-simultaneously, and the same STED laser beam is used for both dyes, the color channels are inherently aligned, and no postprocessing is required.

High-Pressure Freezing. For high-pressure freezing, organs of Corti (p14–p15) were explanted in Hepes-Hanks' solution and placed in aluminum specimen carriers of 200 μm (type A, Leica) depth filled Hepes-Hanks' solution. The aluminum lid (type B, Leica) has been dipped in hexadecen (Sigma-Aldrich) before placing onto the sample. Samples were frozen immediately using the HPM100 (Leica) and rapidly transferred into liquid nitrogen for storage. Freeze substitution was performed in an EM AFS2 (Leica). Samples were incubated for 4 d in 0.1% tannic acid in acetone at −90 °C and subsequently washed three times for 1 h in acetone. Before increasing the temperature from −90 °C to −20 °C (5 °C/h), 2% (wt/vol) osmium tetroxid in acetone was added and incubated for 16 h at −20 °C. Finally, the temperature was raised to 4 °C (10 °C/h) and samples were washed in acetone to remove the osmium tetroxid and warmed to room temperature (RT). Samples were infiltrated and embedded in Epon resin. After the embedding, 250-nm sections for electron tomography were obtained on an Ultracut E ultramicrotome (Leica) with a diamond knife (Diatome). Sections were applied to Formvar-coated copper mesh grids and poststained with 4% (wt/vol) uranyl acetate and Reynold's lead citrate.

Electron Tomography. To both sides of the stained grids, 10-nm gold particles (British Bio Cell) were applied. Single-tilt series were acquired using a JEOL JEM 2100 transmission electron microscope at 200 kV from −60 to +60 with 1° increment, using the Serial-EM software. The tomograms were generated using the IMOD package etomo, and models were rendered using 3dmod (bio3d.colorado.edu/imod/).

Quantitative image analysis was performed blinded, using the ImageJ software package as follows: The height of the ribbon was determined as the maximum extent from the presynaptic density in virtual sections. For ribbon-associated synaptic vesicles, the first row of vesicles with a maximal distance of 80 nm from the ribbon to the vesicle membrane was counted per tomogram. Membrane-proximal synaptic vesicles were defined as vesicles with a membrane-to-membrane distance to the AZ of maximal 50 nm. For tether length analysis, the coordinates of the tether starting (X_1, Y_1, Z_1) and ending (X_2, Y_2, Z_2) points were defined in virtual sections, using the ImageJ software package, and length was calculated according to Tether Length = $\sqrt{((X_2 - X_1)^2 + (Y_2 - Y_1)^2 + (Z_2 - Z_1)^2}$ (see also *SI Appendix*, Fig. S6).

Patch-Clamp and Confocal Ca^{2+} Imaging in IHCs. p14–p16 IHCs from apical coils of freshly dissected organs of Corti were patch-clamped as described (41). The standard pipette solution contained (in mM) 130 Cs-glutamate, 13 TEA-Cl, 20 CsOH·Hepes, 1 $MgCl_2$, 2 MgATP, 0.3 NaGTP, 2 EGTA, 0.4 Fluo-5N (Penta-K^+ salt; Invitrogen), and carboxytetramethyl-rhodamine-conjugated RIBEYE-binding dimer peptide [2 μM (59)] for Ca^{2+} imaging. The pipette solution for perforated patch experiments contained (in mM) 135 Cs-gluconate, 10 TEA-Cl, 10 4-aminopyridine, 10 CsOH·Hepes, 1 $MgCl_2$, and 300 μg/ml amphotericin. The extracellular solution contained (in mM) 104 NaCl, 35 TEA-Cl, 2.8 KCl, 2 $CaCl_2$, 1 $MgCl_2$, 10 NaOH·Hepes, 11.3 D-glucose at pH 7.3. Extracellular [Ca^{2+}] was varied between nominally Ca^{2+}-free to 5 mM for experiments manipulating the single Ca^{2+} channel current and was 10 mM for fluctuation analysis. In all cases, NaCl concentration was adjusted for osmolarity of solutions with different $CaCl_2$ concentrations. Currents were low-pass filtered at 2.9 kHz (8.5 kHz for fluctuation analysis) and sampled at 50 kHz (100 kHz for fluctuation analysis). Cells with holding current greater than −50 pA were discarded. An EPC-9 amplifier and "Pulse" or an EPC-10 amplifier and "Patchmaster" software (HEKA Elektronik) were used for measurements. Whole-cell capacitance measurements were performed in perforated-patch configuration, as previously described (41), except that ΔC_m was estimated as the difference of the mean C_m over 100 ms after the end of the depolarization (the initial 80 ms were skipped). All voltages were corrected for liquid-junction potentials and voltage drops across series resistance. Ca^{2+} currents were further isolated from background current, using a P/n protocol. Confocal Ca^{2+} imaging was performed essentially as described (37). In brief, presynaptic Ca^{2+}-signal of IHCs were observed as changes of Ca^{2+} indicator fluorescence in line scans at the ribbon location, using (20 ms) step depolarizations to −7 mV.

Recordings of Auditory Brainstem Response and Distortion Product Otoacoustic Emissions. Animals aged 5–9 wk were anesthetized intraperitoneally with a combination of ketamine (125 mg/kg) and xylazine (2.5 mg/kg). The core temperature was maintained constant at 37 °C, using a rectal temperature-controlled heating blanket (Hugo Sachs Elektronik-Harvard Apparatus GmbH). For stimulus generation, presentation, and data acquisition, we used the TDT System III (Tucker-Davis-Technologies) run by BioSig32 software (Tucker-Davis-Technologies). Sound pressure levels are provided in dB SPL RMS (tonal stimuli) or dB SPL peak equivalent (PE, clicks) and were calibrated using a 1/4" microphone (D 4039; Brüel and Kjaer GmbH). Tone bursts (12 kHz, 10 ms plateau, 1 ms $\cos^2$ rise/fall, stimulus rate 40 Hz) or clicks of 0.03 ms (stimulus rate 20 and 100 Hz) were presented in the free field ipsilaterally using a JBL 2402 speaker (JBL GmbH & Co.). The difference potential between vertex and mastoid subdermal needles was amplified (50,000 times), filtered (low pass, 4 kHz; high pass, 400 Hz) and sampled at a rate of 50 kHz for 20 ms, 2 × 2,000 times to obtain two mean auditory brainstem response traces for each sound intensity. Hearing threshold was determined with 10 dB precision as the lowest stimulus intensity that evoked a reproducible response waveform in both traces by visual inspection. For distortion product otoacoustic emissions, the ED1/EC1 speaker system (Tucker-Davis-Technologies) was used to generate two primary tones (frequency ratio f2/f1, 1.2; intensity f2 = intensity f1 + 10 dB). Primary tones were coupled into the ear canal by a custom-made probe containing an MKE-2 microphone (Sennheiser) and adjusted to the desired sound intensities at the position of the ear drum, as mimicked in a mouse ear coupler. The microphone signal was amplified and digitalized (Terratec DMX 6 Fire) and analyzed by fast Fourier transformation (Matlab).

Extracellular Recordings from Single. SGNs were performed as previously described (9, 46). In brief, mice aged 4–12 wk were anesthetized by i.p. injection of urethane (1.32 mg·kg^{-1}), xylazine (5 mg·kg^{-1}), and buprenorphine (0.1 mg·kg^{-1}). An occipital approach with partial removal of the cerebellum was taken to advance a glass microelectrode during noise burst stimulation, aiming to identify SGNs near the auditory nerve's entry zone into the cochlear nucleus and avoiding the posterior region of the anteroventral cochlear nucleus, where spherical bushy cells are mainly located. Putative SGNs were distinguished from primary cochlear nucleus units based on the electrode position (electrode aiming at internal auditory canal, >1 mm below the surface of cochlear nucleus) and their primary-like response characteristics to 200 suprathreshold 50-ms tone bursts presented at the characteristic frequency of the SGN, 30 dB above threshold. The irregular firing pattern observed in SGNs was confirmed by a coefficient of variation of interspike intervals of adapted responses greater than 0.5. We first determined the spontaneous rate in a 10-s interval, and if it was below 10 or 2 Hz, an additional 10- or 20-s recording interval was added, respectively. Next, we determined the tuning curve by varying the frequency and intensity of 15-ms tone bursts by an automatically adapting procedure (9). For tuning curves, spike detection was performed online based on a manually set trigger, whereas all other data were analyzed offline using custom-written Matlab routines using waveform-based spike detection. For rate-intensity function, we varied the intensity of 50-ms tone bursts at characteristic frequency (CF) in 5-dB steps between 20 dB below and 50 dB above threshold with 25 repeats for each intensity; the dynamic range was calculated as in ref. 46.

Data Analysis and Statistical Tests. Data are presented as mean ± SEM unless otherwise specified. Normality was assessed with the Jarque-Bera test. *F* test was used to assess equality of variance in normally distributed data sets. The unpaired, two-tailed Wilcoxon rank sum test (also known as Mann-Whitney *U* test) was used to compare data of nonnormal distribution or when variances of experimental groups were unequal. In the case of normally distributed equal-variance data, Student's unpaired two-tailed *t* test was used

to compare two samples (*$P < 0.05$). Comparison of dispersion was performed with a modified Levene's test [Brown-Forsythe test (60)], using median instead of mean for improved robustness under nonnormality. One-way ANOVA followed by Tukey's test was used to detect differences in multiple comparisons for fluctuation analysis. Comparison of ABR thresholds between 6 and 32 kHz and of ABR latencies and amplitudes in response to click stimulation at 10–100 dB was done by two-way ANOVA.

ACKNOWLEDGMENTS. We thank Dr. Kaeser and Dr. Südhof for providing conditional RIM1/2 cDKO mice and Dr. Robbins for providing GFP reporter mice. We thank S. Gerke, C. Senger-Freitag, and N. Herrmann for expert technical assistance; G. Hoch for developing image analysis routines; and Dr. J. Neef for help and discussion. This work was supported by grants from the German Research Foundation: Collaborative Research Center 889 [to T.M. (project A2), N.S. (project A6), and C.W. (project A7)], Center for Molecular Physiology of the Brain Grant FZT-103 (to T.M. and S.W.H.), Priority Program 1608 (to T.M. and N.S.), and Collaborative Research Center 1089 (to S.S.) (projects A01 and P02), as well as the German Federal Ministry of Education and Research (Bernstein Focus for Neurotechnology, 01GQ0810, to T.M.; 01GQ0806 to S.S.), the state of Lower Saxony through "Audiologie-Initiative Niedersachsen" (to T.M.), and Lichtenberg fellowships (to T.O.-T. and A.B.W. through the "Neurosenses" PhD program of the State of Lower Saxony), as well as by local funding (BONFOR to S.S.).

1. Brandt A, Khimich D, Moser T (2005) Few CaV1.3 channels regulate the exocytosis of a synaptic vesicle at the hair cell ribbon synapse. *J Neurosci* 25(50):11577–11585.
2. Frank T, et al. (2010) Bassoon and the synaptic ribbon organize Ca²+ channels and vesicles to add release sites and promote refilling. *Neuron* 68(4):724–738.
3. Zampini V, et al. (2013) Burst activity and ultrafast activation kinetics of CaV1.3 Ca^{2+} channels support presynaptic activity in adult gerbil hair cell ribbon synapses. *J Physiol* 591(Pt 16):3811–3820.
4. Wong AB, et al. (2014) Developmental refinement of hair cell synapses tightens the coupling of Ca2+ influx to exocytosis. *EMBO J* 33(3):247–264.
5. Platzer J, et al. (2000) Congenital deafness and sinoatrial node dysfunction in mice lacking class D L-type Ca2+ channels. *Cell* 102(1):89–97.
6. Brandt A, Striessnig J, Moser T (2003) CaV1.3 channels are essential for development and presynaptic activity of cochlear inner hair cells. *J Neurosci* 23(34):10832–10840.
7. Dou H, et al. (2004) Null mutation of alpha1D Ca2+ channel gene results in deafness but no vestibular defect in mice. *J Assoc Res Otolaryngol* 5(2):215–226.
8. Khimich D, et al. (2005) Hair cell synaptic ribbons are essential for synchronous auditory signalling. *Nature* 434(7035):889–894.
9. Jing Z, et al. (2013) Disruption of the presynaptic cytomatrix protein bassoon degrades ribbon anchorage, multiquantal release, and sound encoding at the hair cell afferent synapse. *J Neurosci* 33(10):4456–4467.
10. Pernia-Andrade A, Jonas P (2011) The multiple faces of RIM. *Neuron* 69(2):185–187.
11. Südhof TC (2012) The presynaptic active zone. *Neuron* 75(1):11–25.
12. Kiyonaka S, et al. (2007) RIM1 confers sustained activity and neurotransmitter vesicle anchoring to presynaptic Ca2+ channels. *Nat Neurosci* 10(6):691–701.
13. Gebhart M, et al. (2010) Modulation of Cav1.3 Ca2+ channel gating by Rab3 interacting molecule. *Mol Cell Neurosci* 44(3):246–259.
14. Kaeser PS, et al. (2011) RIM proteins tether Ca2+ channels to presynaptic active zones via a direct PDZ-domain interaction. *Cell* 144(2):282–295.
15. Coppola T, et al. (2001) Direct interaction of the Rab3 effector RIM with Ca2+ channels, SNAP-25, and synaptotagmin. *J Biol Chem* 276(35):32756–32762.
16. Hibino H, et al. (2002) RIM binding proteins (RBPs) couple Rab3-interacting molecules (RIMs) to voltage-gated Ca(2+) channels. *Neuron* 34(3):411–423.
17. Liu KSY, et al. (2011) RIM-binding protein, a central part of the active zone, is essential for neurotransmitter release. *Science* 334(6062):1565–1569.
18. Han Y, Kaeser PS, Südhof TC, Schneggenburger R (2011) RIM determines Ca²+ channel density and vesicle docking at the presynaptic active zone. *Neuron* 69(2):304–316.
19. Müller M, Liu KSY, Sigrist SJ, Davis GW (2012) RIM controls homeostatic plasticity through modulation of the readily-releasable vesicle pool. *J Neurosci* 32(47):16574–16585.
20. Wang Y, Okamoto M, Schmitz F, Hofmann K, Südhof TC (1997) Rim is a putative Rab3 effector in regulating synaptic-vesicle fusion. *Nature* 388(6642):593–598.
21. Weimer RM, et al. (2006) UNC-13 and UNC-10/rim localize synaptic vesicles to specific membrane domains. *J Neurosci* 26(31):8040–8047.
22. Gracheva EO, Hadwiger G, Nonet ML, Richmond JE (2008) Direct interactions between C. elegans RAB-3 and Rim provide a mechanism to target vesicles to the presynaptic density. *Neurosci Lett* 444(2):137–142.
23. Betz A, et al. (2001) Functional interaction of the active zone proteins Munc13-1 and RIM1 in synaptic vesicle priming. *Neuron* 30(1):183–196.
24. Koushika SP, et al. (2001) A post-docking role for active zone protein Rim. *Nat Neurosci* 4(10):997–1005.
25. Dulubova I, et al. (2005) A Munc13/RIM/Rab3 tripartite complex: From priming to plasticity? *EMBO J* 24(16):2839–2850.
26. Deng L, Kaeser PS, Xu W, Südhof TC (2011) RIM proteins activate vesicle priming by reversing autoinhibitory homodimerization of Munc13. *Neuron* 69(2):317–331.
27. Fernández-Busnadiego R, et al. (2013) Cryo-electron tomography reveals a critical role of RIM1α in synaptic vesicle tethering. *J Cell Biol* 201(5):725–740.
28. Pangršič T, Reisinger E, Moser T (2012) Otoferlin: A multi-C2 domain protein essential for hearing. *Trends Neurosci* 35(11):671–680.
29. Rutherford MA, Pangršič T (2012) Molecular anatomy and physiology of exocytosis in sensory hair cells. *Cell Calcium* 52(3-4):327–337.
30. Safieddine S, El-Amraoui A, Petit C (2012) The auditory hair cell ribbon synapse: From assembly to function. *Annu Rev Neurosci* 35(1):509–528.
31. Ruel J, et al. (2008) Impairment of SLC17A8 encoding vesicular glutamate transporter-3, VGLUT3, underlies nonsyndromic deafness DFNA25 and inner hair cell dysfunction in null mice. *Am J Hum Genet* 83(2):278–292.
32. Seal RP, et al. (2008) Sensorineural deafness and seizures in mice lacking vesicular glutamate transporter 3. *Neuron* 57(2):263–275.
33. Nakamura T, Colbert MC, Robbins J (2006) Neural crest cells retain multipotential characteristics in the developing valves and label the cardiac conduction system. *Circ Res* 98(12):1547–1554.
34. Safieddine S, Wenthold RJ (1999) SNARE complex at the ribbon synapses of cochlear hair cells: Analysis of synaptic vesicle- and synaptic membrane-associated proteins. *Eur J Neurosci* 11(3):803–812.
35. Neef J, et al. (2009) The Ca2+ channel subunit beta2 regulates Ca2+ channel abundance and function in inner hair cells and is required for hearing. *J Neurosci* 29(34):10730–10740.
36. Frank T, Khimich D, Neef A, Moser T (2009) Mechanisms contributing to synaptic Ca2+ signals and their heterogeneity in hair cells. *Proc Natl Acad Sci USA* 106(11):4483–4488.
37. Wong AB, et al. (2013) Concurrent maturation of inner hair cell synaptic Ca2+ influx and auditory nerve spontaneous activity around hearing onset in mice. *J Neurosci* 33(26):10661–10666.
38. Goutman JD, Glowatzki E (2007) Time course and calcium dependence of transmitter release at a single ribbon synapse. *Proc Natl Acad Sci USA* 104(41):16341–16346.
39. Meyer AC, et al. (2009) Tuning of synapse number, structure and function in the cochlea. *Nat Neurosci* 12(4):444–453.
40. Schnee ME, Lawton DM, Furness DN, Benke TA, Ricci AJ (2005) Auditory hair cell-afferent fiber synapses are specialized to operate at their best frequencies. *Neuron* 47(2):243–254.
41. Moser T, Beutner D (2000) Kinetics of exocytosis and endocytosis at the cochlear inner hair cell afferent synapse of the mouse. *Proc Natl Acad Sci USA* 97(2):883–888.
42. Uthaiah RC, Hudspeth AJ (2010) Molecular anatomy of the hair cell's ribbon synapse. *J Neurosci* 30(37):12387–12399.
43. Augustine GJ, Adler EM, Charlton MP (1991) The calcium signal for transmitter secretion from presynaptic nerve terminals. *Ann N Y Acad Sci* 635(1):365–381.
44. Moser T, Predoehl F, Starr A (2013) Review of hair cell synapse defects in sensorineural hearing impairment. *Otol Neurotol* 34(6):995–1004.
45. Liberman MC (1978) Auditory-nerve response from cats raised in a low-noise chamber. *J Acoust Soc Am* 63(2):442–455.
46. Taberner AM, Liberman MC (2005) Response properties of single auditory nerve fibers in the mouse. *J Neurophysiol* 93(1):557–569.
47. Schoch S, et al. (2002) RIM1alpha forms a protein scaffold for regulating neurotransmitter release at the active zone. *Nature* 415(6869):321–326.
48. Schoch S, et al. (2006) Redundant functions of RIM1alpha and RIM2alpha in Ca(2+)-triggered neurotransmitter release. *EMBO J* 25(24):5852–5863.
49. Kintscher M, Wozny C, Johenning FW, Schmitz D, Breustedt J (2013) Role of RIM1α in short- and long-term synaptic plasticity at cerebellar parallel fibres. *Nat Commun* 4:2392.
50. Han Y, Babai N, Kaeser P, Südhof TC, Schneggenburger R (2015) RIM1 and RIM2 redundantly determine Ca2+ channel density and readily releasable pool size at a large hindbrain synapse. *J Neurophysiol* 113(1):255–263.
51. Liang F, et al. (2007) RIM3gamma is a postsynaptic protein in the rat central nervous system. *J Comp Neurol* 503(4):501–510.
52. Alvarez-Baron E, et al. (2013) RIM3γ and RIM4γ are key regulators of neuronal arborization. *J Neurosci* 33(2):824–839.
53. Davydova D, et al. (2014) Bassoon specifically controls presynaptic P/Q-type Ca(2+) channels via RIM-binding protein. *Neuron* 82(1):181–194.
54. Pangršič T, et al. (2015) EF-hand protein Ca2+ buffers regulate Ca2+ influx and exocytosis in sensory hair cells. *Proc Natl Acad Sci USA* 112(9):E1028–E1037.
55. tom Dieck S, et al. (2012) Deletion of the presynaptic scaffold CAST reduces active zone size in rod photoreceptors and impairs visual processing. *J Neurosci* 32(35):12192–12203.
56. Dick O, et al. (2003) The presynaptic active zone protein bassoon is essential for photoreceptor ribbon synapse formation in the retina. *Neuron* 37(5):775–786.
57. Kolmakov K, et al. (2010) Red-emitting rhodamine dyes for fluorescence microscopy and nanoscopy. *Chemistry* 16(1):158–166.
58. Göttfert F, et al. (2013) Coaligned dual-channel STED nanoscopy and molecular diffusion analysis at 20 nm resolution. *Biophys J* 105(1):L01–L03.
59. Francis AA, Mehta B, Zenisek D (2011) Development of new peptide-based tools for studying synaptic ribbon function. *J Neurophysiol* 106(2):1028–1037.
60. Brown MB, Forsythe AB (1974) Robust tests for the equality of variances. *J Am Stat Assoc* 69(346):364–367.